A&A 433, 731–744 (2005)
DOI: 10.1051/0004-6361:20041848

Astronomy & Astrophysics

Benchmarking atomic data for astrophysics: Fe XII*

G. Del Zanna** and H. E. Mason

Department of Applied Mathematics and Theoretical Physics, University of Cambridge, Cambridge, UK
e-mail: G.Del-Zanna@damtp.cam.ac.uk

Received 16 August 2004 / Accepted 20 October 2004

Abstract. We use recently calculated electron collisional data by Storey et al. (2005) for Fe XII ($n = 3$ configurations) to build a model ion to compare to spectroscopic observations of the solar corona and laboratory measurements. We review all the line identifications of the brightest lines, by comparing both wavelengths and line intensities. The presence of blends in different plasma conditions is highlighted. A large number of new energy levels and line identifications are proposed. In particular, we identify the electric quadrupole $^4P^e_{5/2}$–$^4F^e_{9/2}$ transition with the bright coronal line observed at 592.6 Å, previously unidentified. This line, when observed with the 1242.0, 1349.5 UV forbidden lines, is a good density diagnostic over a large range of electron densities. We also indicate the best spectral lines to be used for density diagnostics or instrument calibration. From various combinations of lines we obtain electron densities that are significantly different from those published in the previous literature. Some examples are provided. The agreement between theory and experimental data in terms of wavelengths, line intensities and level lifetimes is excellent.

Key words. atomic data – line: identification

1. Introduction

This paper is another in a series which aims to provide assessed sets of atomic data for the analysis of astrophysical spectra, or benchmark existing datasets against laboratory and solar observations. The approach is observationally based, in the sense that it focuses only on the most important (i.e. brightest) spectral lines that can be observed in solar and laboratory spectra and are useful for plasma diagnostics. The complexities of the benchmark and the types of theoretical and experimental data that are normally available have been described in Del Zanna et al. (2004, hereafter Paper I).

Fe XII is a very important ion because it produces strong spectral lines that can be used both for plasma diagnostics and for instrument calibration. Lines of Fe XII have been recorded by many solar space missions (e.g. Skylab, SOHO), and will be of particular importance for future missions (such as Solar-B).

Storey et al. (2005) have recently calculated new electron collisional data for Fe XII. The new data represent a significant improvement compared to all previous calculations, in particular to the distorted-wave (DW) calculations of Flower (1977) which have been widely used in the literature. Long-standing discrepancies between the electron density values determined from Fe XII when compared with those obtained from other ions have now been solved (Storey et al. 2005). The main problem with the Flower (1977) calculations was an inaccurate target description, hence for some levels an inaccurate mixing was obtained. This in turn affected a few oscillator strengths and collision strengths by more than one order of magnitude, thus also affecting (by the same amount) the cascading to the lower ground levels. Other DW or R-matrix close coupling calculations also had serious deficiencies (see Storey et al. 2005, for references).

There is therefore now scope to use the new collisional data (complemented with new radiative data) to re-assess all line identifications and blends, and the plasma diagnostics that can be obtained with Fe XII. We have done this re-assessment by using the benchmark method described in Paper I and summarised below in Sect. 2. Conclusions and further work needed on this ion are presented in Sect. 5.

2. Method

The method, fully described in Paper I, is very simple. A model ion is built by including all the spectroscopically important configurations and all excitations/ de-excitations between the fine-structure levels. As outlined in Paper I, this is particularly important for complex ions with many metastable levels. The stationary level populations are then solved, obtaining $N_j(N_e, T_e)$, the population of level j relative to the total $N(X^{+r})$ number density of the ion X^{+r}, as a function of the electron temperature and density. The line intensities, Ith, which are

* The full datasets of energies (Table 2) and radiative data (Table 3) are only available in electronic form at the CDS via anonymous ftp to cdsarc.u-strasbg.fr (130.79.128.5) or via http://cdsweb.u-strasbg.fr/cgi-bin/qcat?J/A+A/433/731

** *Present address*: MSSL, University College London, Holmbury St. Mary Dorking, Surrey RH5 6NT, UK.

proportional to $N_j A_{ji}$, are then directly obtained, knowing A_{ji}, the spontaneous transition probability from the upper level j to the lower level i. The brightest lines are then considered, and the line identifications reviewed using this model ion, and a comprehensive set of experimental data. The ratios between theoretical and observed line intensities (scaled with the electron density N_e):

$$F_{ji} = \frac{I_{ob} N_e}{N_j(N_e, T_0)\, A_{ji}} \quad (1)$$

are then calculated (at a fixed temperature T_0) and plotted as a function of the electron density N_e. If agreement between theory and observations is present, all the "emissivity ratio curves" F_{ji} will either overlap or cross at one density value. Note that this approach is the same as analysing all the possible combinations of line ratios, as has been done in almost all earlier publications on the subject. A plot of F_{ji} curves has the advantage of giving a global view of all the lines at once, and clearly shows which lines are best for calibration and which are best for density diagnostic purposes (in the latter case it also shows over which density regimes the diagnostic lines can be used).

Temperature effects can be important for some ions and some combination of lines, but are normally second order effects, compared to the uncertainties in the line identifications, line blending, instrument calibration, and in the atomic data. For Fe XII, the F_{ji} curves have been calculated at $\log T_0$ [K] = 6.15, the temperature of peak emission in ionization equilibrium, and normalised to an arbitrary constant.

The energy levels are semi-empirically adjusted using the identified transitions. These are then used to re-calculate the radiative data using the SUPERSTRUCTURE program (SS, see Eissner et al. 1974; Nussbaumer & Storey 1978). In particular, we adopt the semi-empirical Term Energy Correction (TEC) procedure (see, e.g. Zeippen et al. 1977; Nussbaumer & Storey 1978), where empirical corrections to the LS energies are introduced in the calculations, to obtain empirically-adjusted fine-structure energies, E_{SS}. If more than one fine-structure level has a known energy, an average for the LS term is used. For uncertain levels, the same corrections are applied as those for other levels which have the same parent term.

The adjusted energies E_{SS} are then compared to the observed energies E_{obs}, which are directly derived from the observed wavelengths. The uncertainties in the energies reflect the estimated uncertainties in the observed wavelengths. Ground-based measurements have been converted to vacuum wavelengths using the standard formula for the refractive index of air given by Edlén (1966).

Normally a few trial adjustments are necessary, before a suitable and consistent set of energies can be obtained. At the end of the iterative procedure, a set of best energies E_{best} is provided. These energies are the observed energies, whenever available, and the adjusted E_{SS} values otherwise.

One of the important results of the process is the possibility to check that the energies obtained from the scattering calculation E_{CC} are in the right order and have the correct energy differences. If this does not hold, the resulting collision strengths are likely to be inaccurate, as often occurs in the literature. Strong level mixing is present in all the Fe coronal ions. This often complicates the effect of the corrections to the LS energies and the level assignments, in particular when some of the levels have unknown energies.

To calculate transition probabilities, it is important, in particular for the magnetic quadrupole (M2) and electric quadrupole (E2) cases, to use experimental energies and not the theoretical ones. Accurate A-values are also needed for *all* the transitions in order to build the ion model. In this paper, the iterative procedure outlined above is implemented, in order to obtain the best energies and line strengths. Then, the best energies E_{best} are used to calculate the A-values of all the E1, E2, M1, and M2 transitions in intermediate coupling with SUPERSTRUCTURE.

The ion level balance has been calculated using all the collisional and radiative data between the levels. Proton excitations and photo-excitations can be important processes for the forbidden transitions taking place between levels within the same configuration. We have used here the proton rates calculated by Landman (1978) as included in CHIANTI version 4 (Young et al. 2003). However, the addition of these two processes only slightly affect the Fe XII level balance, for the observations considered here.

2.1. Line identifications

In the literature, the most common reference values used are the observed energies E_{obs} and wavelengths available from the National Institute of Science and Technology (NIST) Atomic Spectra Database (see Fuhr et al. 1999). NIST is a large compilation of published values that is not always complete or up-to-date. For important coronal ions such as Fe XII and Fe XI, many of the fine-structure level energies are not known, or only known relative to particular levels within a configuration. Therefore, many lines are still unidentified or have conflicting identifications in the literature.

Even the most comprehensive and recent ab initio calculations are not good enough to match the observations, and the predicted wavelengths are often inaccurate by a few Å. Many of the identifications in the past have been based either on the variations of the wave number intervals along isoelectronic sequences (together with gf values), or on approximate estimates of line intensities. This method, pioneered by B. Edlen, has been very successful, but is difficult to apply to the weaker transitions, and those originating from highly-mixed levels. In the present series, all the observed level energies are re-assessed, by re-considering the original solar and laboratory measurements, and by using the latest atomic data.

3. Experimental data

There are a large number of laboratory and solar spectroscopic observations of Fe XII lines. However, very few published studies can be used for the present benchmark (for a review see Paper I). In fact, only a few studies had sufficient spectral resolution, completeness (in wavelength coverage) and reported calibrated line intensity measurements. Only a few of these

Table 1. The configurations used to calculate the radiative data.

c1: $3s^2\ 3p^3$	c2: $3s\ 3p^4$	c3: $3s^2\ 3p^2\ 3d$	c4: $3p^5$
c5: $3s\ 3p^3\ 3d$	c6: $3p^4\ 3d$	c7: $3s\ 3p^2\ 3d^2$	c8: $3p^3\ 3d^2$
c9: $3s^2\ 3p\ 3d^2$	c10: $3s^2\ 3d^3$	c11: $3s\ 3p\ 3d^3$	c12: $3p^2\ 3d^3$
c13: $3s^2\ 3p^2\ 4s$	c14: $3s^2\ 3p^2\ 4p$	c15: $3s^2\ 3p^2\ 4d$	c16: $3s^2\ 3p^2\ 4f$
c17: $3s\ 3p^3\ 4s$	c18: $3s\ 3p^3\ 4p$	c19: $3s\ 3p^3\ 4d$	c20: $3s\ 3p^3\ 4f$
c21: $3p^4\ 4s$	c22: $3p^4\ 4p$	c23: $3p^4\ 4d$	c24: $3p^4\ 4f$

were radiometrically calibrated in a way that is independent of the atomic data, and are therefore of limited use for the present benchmark.

3.1. Solar spectra

The solar observations are best for the identification of spectral lines that form in low-density plasmas, in particular for the forbidden lines, but also for the weak dipole-allowed transitions. In this paper, for the wavelengths of the allowed transitions we mainly use the accurate values of Behring et al. (1976) [hereafter Be76], who provided a whole-Sun spectrum in the 160−770 Å range with excellent resolution (0.06 Å). For the intensities, we use the approximate values given by Be76 (but only for lines close in wavelength), and the photometrically-calibrated spectrum of Malinovsky & Heroux (1973). The latter still represent the best available medium-resolution (0.25 Å) integrated-Sun spectrum in the 150−300 Å range, with uncertainties in the relative radiometric calibration of the order of 10−20% for lines which are close in wavelength. The tables provided by Malinovsky & Heroux (1973) were not complete, so we have scanned their spectrum in order to provide additional information.

We also use spectra from the Solar and Heliospheric Observatory (SOHO) Coronal Diagnostic Spectrometer (CDS). The CDS covers a wide wavelength range (150−780 Å), with nine channels (six in first order), distributed between a Normal Incidence (NIS) and a Grazing Incidence (GIS) Spectrometer. Here we use the CDS calibration of Del Zanna et al. (2001).

Finally, we use data from the Goddard Solar Extreme Ultraviolet Rocket Telescope and Spectrograph (SERTS). The various rocket spectra have produced data of excellent spectral resolution. Here, we only use the most reliable radiometrically-calibrated data, from part of the first-order (235−450 Å) spectrum of the SERTS-89 (Thomas & Neupert 1994) flight.

3.1.1. Coronal forbidden lines

Very few observations of coronal forbidden lines exist. These observations are however very important because energy level separations can be measured with high accuracy ($\simeq$1 cm^{-1}). In the visible, we use the solar eclipse observations of Jefferies et al. (1971). For the UV, we mainly use the wavelengths and the calibrated line intensities in the 970–2650 Å range reported by Sandlin et al. (1977) and observed with the Skylab ATM NRL S082B spectrograph. The authors estimated the relative intensities to be accurate within 30% in the 1210–1930 Å range and 50% above 1930 Å, given the large scattered continuum. The wavelengths are accurate to within $\simeq$0.01 Å. Feldman & Doschek (1977) provided a list of forbidden lines in the 1170−2650 Å range. We also use data for the UV forbidden lines observed with the Harvard Skylab spectrometer and presented by Vernazza & Reeves (1978).

Coronal forbidden lines have also been observed with the SOHO Solar UV Measurement of Emitted Radiation (SUMER) instrument in the in the 500−1600 Å range. Here we have used the off-limb observations described by Feldman et al. (1997). These authors did not provide integrated line intensities, and we have therefore re-analysed the same dataset in order to obtain calibrated line intensities. The data have been processed using the standard SolarSoft[1] SUMER software and radiometric calibration. Integrated line counts were calculated over an average spectrum obtained from a central portion of the field of view, located approximately 30″ off-limb.

3.2. Laboratory data in the XUV-visible

Most Fe XII identifications have been based on plates taken at the Culham laboratory in the UK (see, e.g. Fawcett et al. 1967; Fawcett 1971; Bromage et al. 1978). These laboratory spectra were not free from impurities, but had an excellent resolution and are best for identifying lines that are formed in high-density plasmas. We have used the original plates and some unpublished material (B. Fawcett, priv. comm.) in the present assessment.

More recently, papers based on beam-foil spectroscopy or electron beam ion traps have produced very useful spectral data for the identifications of Fe XII lines. Here, we use data from Jupen et al. (1993), Trabert (1998), Träbert et al. (2003). Another important contribution of these laboratory studies is the measurement of lifetimes and A values. Here, we use the measurements of Moehs et al. (2001) and Träbert et al. (2002).

4. Model ion for Fe XII

We restrict our discussion to the main $n = 3$ spectroscopic configurations in Fe XII, (c1: $3s^2\ 3p^3$, c2: $3s\ 3p^4$, c3: $3s^2 3p^2\ 3d$), which produce 41 fine-structure levels, and the majority of the brightest lines. For the calculations we have actually included the $3p^5$ (c4) and $3s\ 3p^3\ 3d$ (c5) configurations, for a total of 143 fine-structure levels. To calculate the radiative data for all transitions among these 143 levels we have used the same set of 24 configurations (set 3) described by Binello et al. (2001), also

[1] www.lmsal.com/solarsoft/

listed in Table 1. The "standard" scaled Thomas-Fermi-Dirac potentials were adopted to approximate the radial parts of the wavefunctions. The scaling parameters for the potential employed in the calculation are: λ(1s) = 1.4108; λ(2s) = 1.1162; λ(2p) = 1.0626; λ(3s) = 1.1504; λ(3p) = 1.1236; λ(3d) = 1.1337; λ(4s) = 1.1743; λ(4p) = 1.1413; λ(4d) = 1.1594; λ(4f) = 1.3355.

The method outlined in Sect. 2 was applied iteratively a few times, using the *R*-matrix collisional data of Storey et al. (2005) and the *A* values calculated with SUPERSTRUCTURE and the best energies. Table 2 lists the results for the 41 levels (and a few significant 3s $3p^3$ 3d levels), ordered according to the energies $E_{\rm CC}$ of the collisional calculations. This table also lists SS level mixing information, together with the energies $E_{\rm best}$ which we propose in this paper to be the best set. For comparisons, the $E_{\rm NIST}$ values reported in NIST are also listed.

4.1. Benchmarking A values

Table 3 presents the radiative data[2] (gf and A values) for the brightest transitions. The improvement in the target presented here only produced minor changes in the A values, when compared to the values calculated by Binello et al. (2001), due to the different term energy corrections and observed energies. The differences with the compiled values in NIST are small (about 10%) for the brightest transitions.

The lifetimes of a few levels have been measured and these values are compared with our predicted values in Table 4. The agreement is excellent, in particular with the later and more accurate results of Träbert et al. (2002).

4.2. Energy levels and line identifications

A discussion of the main spectral identifications for each of the levels is essential in our procedure. It is virtually impossible to provide details for all the line identifications proposed, discussed, or rejected in the literature. We note that in published line lists a large number of lines have been incorrectly identified or did not take into account blending. In what follows we present the most important points. A summary of the proposed identifications, compared to previous ones (whenever present) is given in Table 5. In Table 5 we normally list only the first publication that positively identified each transition.

Note that a large number of transitions have been identified in the laboratory spectra where electron densities are much higher than the solar corona. Some of these lines are also visible in solar spectra, but others are not. On the other hand, there are many lines that are only visible at low densities. As a guideline, we provide in Table 5 the intensities of all the brightest transitions calculated at low (10^8 cm^{-3}) and high-densities (10^{12} cm^{-3}).

Some of the lines are self-blended or blend with transitions from other ions, the most common ones in solar spectra are indicated in the table. However note that blending depends on the instrument resolution and on the plasma source. Transitions that are obviously blended with lines from other ions cannot be identified/benchmarked with certainty, and have a question mark in Table 5. Note that, due to the lack of radiometrically-calibrated high-resolution quiet-Sun data in the 200−250 Å range, we are unable to identify many transitions with certainty. Hence we cannot assign accurate energies to the corresponding levels.

4.2.1. The forbidden transitions within the ground $3s^2\ 3p^3$ configuration

Transitions within the $3s^2\ 3p^3$ configuration produce very bright forbidden lines in the UV spectra of the solar corona. For the energies of the ground configuration we have adopted the Sandlin et al. (1977) wavelength measurements (see Table 5), which are fully consistent with the energy differences derived from measurements of the EUV lines, and in agreement with the values reported by Feldman & Doschek (1977). We note that energies (see Table 2) and vacuum wavelengths (see Table 3) listed by NIST are at odds with the observed wavelengths.

At shorter wavelengths, only two spectral lines (1−5 1242.0 Å; 1−4 1349 Å) have been observed in solar off-limb or on-disc observations, and in stellar spectra. We find good agreement with the Skylab off-limb observations of Sandlin et al. (1977) and Vernazza & Reeves (1978), as Figs. 1 and 2 show. In on-disc observations, these lines become weak (because of the continuum) and difficult to observe (except in flares). With the Skylab Harvard spectrometer, the 1242.0 Å line is blended with a strong N V line on-disc.

In previous literature, the 1242, 1349 Å lines have been used for density diagnostics of solar (e.g. Cook et al. 1994) and stellar (e.g. Jordan et al. 2001) coronae. We note that according to our model these lines are good density diagnostics only for densities higher than 10^{10} cm^{-3} (see also Figs. 1 and 2). At low densities, the ratio of the 1242, 1349 Å lines is predicted to be 1.7, stay approximately constant until 10^{10} cm^{-3}, and then increase to 3.9 at 10^{12} cm^{-3}. This is in stark contrast to the theoretical results of Cook et al. (1994), where the low-density limit was instead at much lower densities ($\simeq 10^7$ cm^{-3}).

Table 6 presents a collection of measurements of the 1242, 1349 Å ratio (and densities derived from it with the present model) from the literature, with the addition of SOHO SUMER off-limb measurements analysed here. With the exception of the far off-limb measurements (from both Skylab and SOHO/SUMER), for which the measured values are slightly below our low-density limit, the values and the densities are reasonable. The densities we obtain from the active region and flare observations reported by Cook et al. (1994) are much higher than the values derived by the authors, and in better agreement with typical values obtained from other ions. For example, for a flare observation (ratio 1242, 1349 Å = 2.85) we obtain 3.8×10^{10} cm^{-3}, while Cook et al. (1994) obtained 5.9×10^9 cm^{-3}. Jordan et al. (2001) measured with the HST/STIS instrument a ratio (ergs) of approximately 2, which gives a rather low density.

[2] The complete dataset, together with level energies, is available on-line.

Table 2. Energy levels for the main three configurations in Fe XII, plus a few significant ones from the 3s $3p^3$ 3d configuration. The percentage of level mixing (>10%) is indicated in second column. E_{best} indicates the best energies (cm^{-1}) which we propose in this work. The uncertainties in the energies reflect the estimated errors in the wavelength measurements. Levels with uncertain identification are assigned an uncertainty of 500 cm^{-1}. The following columns indicate the differences between our E_{best} and the energies from NIST E_{NIST}, the collisional calculations E_{CC}, and the adjusted SS values E_{SS}. Levels are ordered according to the energies E_{CC} from the collisional calculations.

i	Configuration (% purity)	Term	E_{best}	$E_{best} - E_{NIST}$	$E_{best} - E_{CC}$	$E_{best} - E_{SS}$
1	$3s^2\ 3p^3$(93%)	$^4S^o_{3/2}$	0.0 ± 0	0	+0	0
2	$3s^2\ 3p^3$(84%) +5(10%)	$^2D^o_{3/2}$	41 555.6 ± 1	–10.4	−2845	−28
3	$3s^2\ 3p^3$(96%)	$^2D^o_{5/2}$	46 088.0 ± 1	13	−2732	−117
4	$3s^2\ 3p^3$(95%)	$^2P^o_{1/2}$	74 107.0 ± 1	–2	−2522	−148
5	$3s^2\ 3p^3$(82%) +2(11%)	$^2P^o_{3/2}$	80 515.0 ± 1	0	−2052	−190
6	$3s\ 3p^4$(87%)	$^4P^e_{5/2}$	274 373.0 ± 5	0	+840	+55
7	$3s\ 3p^4$(87%)	$^4P^e_{3/2}$	284 005.0 ± 5	0	+1212	−46
8	$3s\ 3p^4$(86%)	$^4P^e_{1/2}$	288 307.0 ± 5	0	+1245	−83
9	$3s\ 3p^4$(75%) +33(c3 19%)	$^2D^e_{3/2}$	339 725.0 ± 30	–295	−1847	−101
10	$3s\ 3p^4$(76%) +34(c3 19%)	$^2D^e_{5/2}$	341 716.0 ± 10	13	−1656	−96
11	$3s\ 3p^4$(45%) +26(c3 44%)	$^2P^e_{3/2}$	389 719.0 ± 20	13	−4335	−169
12	$3s\ 3p^4$(32%) +28(c3 28%) +13(28%)	$^2P^e_{1/2}$	394 360.0 ± 20	240	−4298	−135
13	$3s\ 3p^4$(52%) +12(14%) +28(c3 17%)	$^2S^e_{1/2}$	410 401.0 ± 20	–	−3589	−94
14	$3s^2\ 3p^2\ (^3P)\ 3d$(92%)	$^4F^e_{3/2}$	426 920.0 ± 100	–	−5996	−845
15	$3s^2\ 3p^2\ (^3P)\ 3d$(90%)	$^4F^e_{5/2}$	430 758.0 ± 100	–	−5868	−776
16	$3s^2\ 3p^2\ (^3P)\ 3d$(91%)	$^4F^e_{7/2}$	436 088.0 ± 100	–	−5990	−978
17	$3s^2\ 3p^2\ (^1D)\ 3d$(44%) +36(30%) +22(20%)	$^2F^e_{5/2}$	443 318.0 ± 500	–	−6050	0
18	$3s^2\ 3p^2\ (^3P)\ 3d$(94%)	$^4F^e_{9/2}$	443 121.0 ± 30	–	−5807	−771
19	$3s^2\ 3p^2\ (^1D)\ 3d$(46%) +39(17%) +23(30%)	$^4D^e_{7/2}$	447 070.0 ± 50	–	−6081	−276
20	$3s^2\ 3p^2\ (^3P)\ 3d$(95%)	$^4D^e_{1/2}$	446 977.0 ± 500	–	−5318	0
21	$3s^2\ 3p^2\ (^3P)\ 3d$(92%)	$^4D^e_{3/2}$	448 071.0 ± 500	–	−5366	0
22	$3s^2\ 3p^2\ (^3P)\ 3d$(68%) +17(12%)	$^4D^e_{5/2}$	451 651.0 ± 100	–	−6440	−958
23	$3s^2\ 3p^2\ (^3P)\ 3d$(28%) +39(19%) +19(45%)	$^2F^e_{7/2}$	461 474.0 ± 100	–	−6204	−693
24	$3s^2\ 3p^2\ (^1D)\ 3d$(94%)	$^2G^e_{7/2}$	494 518.0 ± 200	–	−9374	−41
25	$3s^2\ 3p^2\ (^1D)\ 3d$(94%)	$^2G^e_{9/2}$	497 256.0 ± 300	–	−9596	−329
26	$3s^2\ 3p^2\ (^3P)\ 3d$(25%) +11(c2 43%) +37(23%)	$^2P^e_{3/2}$	501 800.0 ± 30	0	−8406	−67
27	$3s^2\ 3p^2\ (^3P)\ 3d$(83%)	$^4P^e_{5/2}$	512 508.0 ± 5	–2	−9186	−394
28	$3s^2\ 3p^2\ (^3P)\ 3d$(21%) +12(c2 38%) +35(28%)	$^2P^e_{1/2}$	513 850.0 ± 10	–	−8003	−38
29	$3s^2\ 3p^2\ (^3P)\ 3d$(80%)	$^4P^e_{3/2}$	516 772.0 ± 5	–	−8847	−112
30	$3s^2\ 3p^2\ (^3P)\ 3d$(80%)	$^4P^e_{1/2}$	519 767.0 ± 5	–3	−8350	+206
31	$3s^2\ 3p^2\ (^1S)\ 3d$(42%) +41(35%)	$^2D^e_{3/2}$	526 127.0 ± 10	7	−9423	−236
32	$3s^2\ 3p^2\ (^1S)\ 3d$(27%) +40(36%) +34(20%)	$^2D^e_{5/2}$	536 939.0 ± 10	–1101	−9571	−170
33	$3s^2\ 3p^2\ (^1D)\ 3d$(57%) +9(c2 14%) +31(21%)	$^2D^e_{3/2}$	553 906.0 ± 5	–124	−9921	+118
34	$3s^2\ 3p^2\ (^1D)\ 3d$(37%) +32(48%)	$^2D^e_{5/2}$	554 632.0 ± 5	22	−10 101	−348
35	$3s^2\ 3p^2\ (^1D)\ 3d$(52%) +28(19%) +38(17%)	$^2P^e_{1/2}$	569 794.0 ± 50	854	−12 763	−5
36	$3s^2\ 3p^2\ (^3P)\ 3d$(47%) +17(34%)	$^2F^e_{5/2}$	576 733.0 ± 10	–7	−12 510	−198
37	$3s^2\ 3p^2\ (^1D)\ 3d$(62%) +26(25%)	$^2P^e_{3/2}$	577 680.0 ± 20	–60	−12 854	−319
38	$3s^2\ 3p^2\ (^1D)\ 3d$(60%) +35(10%) +13(c2 11%)	$^2S^e_{1/2}$	576 153.0 ± 20	–3477	−12 652	−323
39	$3s^2\ 3p^2\ (^3P)\ 3d$(59%) +23(36%)	$^2F^e_{7/2}$	581 171.0 ± 20	–9	−12 454	−218
40	$3s^2\ 3p^2\ (^3P)\ 3d$(50%) +32(15%) +34(12%)	$^2D^e_{5/2}$	603 940.0 ± 20	10	−12 474	−167
41	$3s^2\ 3p^2\ (^3P)\ 3d$(58%) +31(27%)	$^2D^e_{3/2}$	605 540.0 ± 50	60	−12 441	−75
50	$3s\ 3p^3\ 3d$(40%) +84(38%)	$^4D^o_{7/2}$	663 573.0 ± 500	–	−20 284	0
72	$3s\ 3p^3\ 3d$(51%) +74(14%) +84(13%)	$^4D^o_{7/2}$	761 930.0 ± 500	–	−19 935	0
74	$3s\ 3p^3\ 3d$(76%)	$^4F^o_{7/2}$	765 403.0 ± 500	–	−21 016	0
84	$3s\ 3p^3\ 3d$(32%) +50(33%) +72(11%) +139(c9 10%)	$^4D^o_{7/2}$	797 914.0 ± 500	–	−20 297	0
119	$3s^2\ 3p\ 3d^2$(52%) +139(21%)	$^4D^o_{7/2}$	935 897.0 ± 500	–	−21 879	0
139	$3s^2\ 3p\ 3d^2$(56%) +119(22%)	$^4D^o_{7/2}$	989 745.0 ± 500	–	−22 430	0

Table 3. Results for the brightest lines in Fe XII. The lines are grouped in different transition arrays, and are displayed in decreasing order of intensity. Columns 2, 3 show the relative line intensities (photons) $Int = N_j A_{ji}/N_e$ calculated at $\log T[\mathrm{K}] = 6.15$ and 10^8, 10^{12} cm^{-3}, normalised to the intensity of the brightest line. Columns 4, 5 show the gf and A values calculated in this work. Column 6 shows, for comparison, the NIST A values. The last two columns show the wavelengths corresponding to the best energies E_{best} of Table 2 and the NIST vacuum wavelengths. The uncertainties on the proposed wavelengths are derived from the uncertainties assigned to the energies.

$i-j$	Int	Int	gf	A_{ji}	A_{ji}	T	Terms	λ_{best}(Å)	λ(Å)
	10^8	10^{12}			NIST				NIST
1–2	0.32	1.7×10^{-3}	–	56.	48.	M1	c1 $^4S^o_{3/2}$–c1 $^2D^o_{3/2}$	2406.41 ± 0.06	2405.81
1–3	0.19	1.2×10^{-4}	–	2.3	1.7	M1	c1 $^4S^o_{3/2}$–c1 $^2D^o_{5/2}$	2169.76 ± 0.05	2170.37
1–5	5.6×10^{-2}	7.5×10^{-3}	–	3.5×10^{2}	3.2×10^{2}	M1	c1 $^4S^o_{3/2}$–c1 $^2P^o_{3/2}$	1242.01 ± 0.01	1242.00
1–4	3.2×10^{-2}	2.1×10^{-3}	–	1.9×10^{2}	1.8×10^{2}	M1	c1 $^4S^o_{3/2}$–c1 $^2P^o_{1/2}$	1349.40 ± 0.02	1349.36
2–5	3.2×10^{-2}	4.4×10^{-3}	–	2.0×10^{2}	2.0×10^{2}	M1	c1 $^2D^o_{3/2}$–c1 $^2P^o_{3/2}$	2566.77 ± 0.13	2567.46
3–5	1.3×10^{-2}	1.8×10^{-3}	–	82.	80.	M1	c1 $^2D^o_{5/2}$–c1 $^2P^o_{3/2}$	2904.70 ± 0.17	2903.6
2–4	1.2×10^{-2}	8.0×10^{-4}	–	72.	70.	M1	c1 $^2D^o_{3/2}$–c1 $^2P^o_{1/2}$	3072.06 ± 0.19	3072.9
18–25	1.1×10^{-3}	1.7×10^{-4}	–	1.2×10^{2}	–	M1	c3 $^4F^e_{9/2}$–c3 $^2G^e_{9/2}$	1847.23 ± 11.19	–
16–18	4.5×10^{-3}	2.7×10^{-5}	–	12.	–	M1	c3 $^4F^e_{7/2}$–c3 $^4F^e_{9/2}$	14 218.68 ± 258.05	–
6–18	2.3×10^{-2}	1.4×10^{-4}	–	62.	–	E2	c2 $^4P^e_{5/2}$–c3 $^4F^e_{9/2}$	592.600 ± 0.123	–
1–6	0.31	0.12	0.20	1.7×10^{9}	1.6×10^{9}	E1	c1 $^4S^o_{3/2}$–c2 $^4P^e_{5/2}$	364.467 ± 0.007	364.467
1–7	0.18	7.3×10^{-2}	0.14	1.8×10^{9}	1.7×10^{9}	E1	c1 $^4S^o_{3/2}$–c2 $^4P^e_{3/2}$	352.106 ± 0.006	352.106
1–8	9.0×10^{-2}	3.5×10^{-2}	6.9×10^{-2}	1.9×10^{9}	1.8×10^{9}	E1	c1 $^4S^o_{3/2}$–c2 $^4P^e_{1/2}$	346.852 ± 0.006	346.852
3–11	2.5×10^{-2}	8.4×10^{-2}	0.40	7.8×10^{9}	–	E1	c1 $^2D^o_{5/2}$–c2 $^2P^e_{3/2}$	291.010 ± 0.018	–
3–10	2.3×10^{-2}	9.6×10^{-2}	0.29	2.9×10^{9}	2.9×10^{9}	E1	c1 $^2D^o_{5/2}$–c2 $^2D^e_{5/2}$	338.263 ± 0.013	338.263
2–9	1.6×10^{-2}	6.7×10^{-2}	0.23	3.5×10^{9}	3.5×10^{9}	E1	c1 $^2D^o_{3/2}$–c2 $^2D^e_{3/2}$	335.380 ± 0.035	335.060
2–12	6.0×10^{-3}	3.3×10^{-2}	0.18	7.4×10^{9}	–	E1	c1 $^2D^o_{3/2}$–c2 $^2P^e_{1/2}$	283.443 ± 0.017	–
5–13	4.5×10^{-3}	3.1×10^{-2}	0.21	7.5×10^{9}	–	E1	c1 $^2P^o_{3/2}$–c2 $^2S^e_{1/2}$	303.135 ± 0.019	–
1–27	1.0	0.32	2.91	8.5×10^{10}	8.6×10^{10}	E1	c1 $^4S^o_{3/2}$–c3 $^4P^e_{5/2}$	195.119 ± 0.002	195.119
1–29	0.67	0.21	1.95	8.7×10^{10}	9.1×10^{10}	E1	c1 $^4S^o_{3/2}$–c3 $^4P^e_{3/2}$	193.509 ± 0.002	193.509
1–30	0.32	0.10	0.96	8.7×10^{10}	9.0×10^{10}	E1	c1 $^4S^o_{3/2}$–c3 $^4P^e_{1/2}$	192.394 ± 0.002	192.394
3–39	5.3×10^{-2}	0.31	4.44	1.1×10^{11}	1.0×10^{11}	E1	c1 $^2D^o_{5/2}$–c3 $^2F^e_{7/2}$	186.887 ± 0.007	186.880
3–32	3.2×10^{-2}	8.7×10^{-2}	1.09	2.9×10^{10}	–	E1	c1 $^2D^o_{5/2}$–c3 $^2D^e_{5/2}$	203.728 ± 0.005	–
3–16	4.0×10^{-2}	2.6×10^{-2}	1.9×10^{-3}	2.4×10^{7}	–	E1	c1 $^2D^o_{5/2}$–c3 $^4F^e_{7/2}$	256.410 ± 0.066	–
3–19	2.6×10^{-2}	4.1×10^{-2}	2.3×10^{-3}	3.1×10^{7}	–	E1	c1 $^2D^o_{5/2}$–c3 $^4D^e_{7/2}$	249.388 ± 0.032	–
3–34	1.8×10^{-2}	0.12	1.44	4.1×10^{10}	4.9×10^{10}	E1	c1 $^2D^o_{5/2}$–c3 $^2D^e_{5/2}$	196.640 ± 0.002	196.640
1–22	1.9×10^{-2}	1.6×10^{-2}	1.4×10^{-2}	3.1×10^{8}	–	E1	c1 $^4S^o_{3/2}$–c3 $^4D^e_{5/2}$	221.410 ± 0.049	–
3–23	2.0×10^{-2}	2.7×10^{-2}	1.2×10^{-5}	1.8×10^{5}	–	E1	c1 $^2D^o_{5/2}$–c3 $^2F^e_{7/2}$	240.740 ± 0.059	–
3–26	1.7×10^{-2}	0.12	1.29	4.5×10^{10}	–	E1	c1 $^2D^o_{5/2}$–c3 $^2P^e_{3/2}$	219.437 ± 0.015	–
3–27	1.6×10^{-2}	5.2×10^{-3}	5.7×10^{-2}	1.4×10^{9}	1.1×10^{9}	E1	c1 $^2D^o_{5/2}$–c3 $^4P^e_{5/2}$	214.399 ± 0.003	214.39
2–30	1.5×10^{-2}	5.0×10^{-3}	5.5×10^{-2}	4.2×10^{9}	1.8×10^{9}	E1	c1 $^2D^o_{3/2}$–c3 $^4P^e_{1/2}$	209.113 ± 0.003	209.12
1–17	1.5×10^{-2}	2.9×10^{-2}	4.8×10^{-3}	1.1×10^{8}	–	E1	c1 $^4S^o_{3/2}$–c3 $^2F^e_{5/2}$	225.572 ± 0.254	–
2–14	1.6×10^{-2}	9.9×10^{-3}	6.8×10^{-3}	1.7×10^{8}	–	E1	c1 $^2D^o_{3/2}$–c3 $^4F^e_{3/2}$	259.495 ± 0.068	–
2–31	1.2×10^{-2}	1.7×10^{-2}	0.21	8.2×10^{9}	–	E1	c1 $^2D^o_{3/2}$–c3 $^2D^e_{3/2}$	206.368 ± 0.005	–
2–36	1.0×10^{-2}	0.19	3.12	9.9×10^{10}	–	E1	c1 $^2D^o_{3/2}$–c3 $^2F^e_{5/2}$	186.854 ± 0.004	–
5–40	5.0×10^{-3}	0.14	2.96	9.0×10^{10}	–	E1	c1 $^2P^o_{3/2}$–c3 $^2D^e_{5/2}$	191.049 ± 0.008	–
2–33	3.9×10^{-3}	9.1×10^{-2}	1.30	5.7×10^{10}	6.1×10^{10}	E1	c1 $^2D^o_{3/2}$–c3 $^2D^e_{3/2}$	195.179 ± 0.002	195.14
3–24	1.9×10^{-3}	1.7×10^{-2}	1.5×10^{-2}	2.5×10^{8}	–	E1	c1 $^2D^o_{5/2}$–c3 $^2G^e_{7/2}$	223.000 ± 0.100	–
5–37	1.5×10^{-3}	6.4×10^{-2}	1.24	5.1×10^{10}	5.1×10^{10}	E1	c1 $^2P^o_{3/2}$–c3 $^2P^e_{3/2}$	201.140 ± 0.008	201.121
2–34	9.3×10^{-4}	6.2×10^{-3}	7.5×10^{-2}	2.2×10^{9}	1.7×10^{9}	E1	c1 $^2D^o_{3/2}$–c3 $^2D^e_{5/2}$	194.903 ± 0.002	194.920
3–33	6.7×10^{-4}	1.6×10^{-2}	0.23	9.7×10^{9}	1.1×10^{10}	E1	c1 $^2D^o_{5/2}$–c3 $^2D^e_{3/2}$	196.921 ± 0.002	196.923
4–37	5.4×10^{-4}	2.3×10^{-2}	0.44	1.9×10^{10}	1.6×10^{10}	E1	c1 $^2P^o_{1/2}$–c3 $^2P^e_{3/2}$	198.581 ± 0.008	198.555
4–33	4.3×10^{-4}	9.9×10^{-3}	0.16	6.2×10^{9}	6.7×10^{9}	E1	c1 $^2P^o_{1/2}$–c3 $^2D^e_{3/2}$	208.421 ± 0.003	208.37
6–84	1.8×10^{-2}	7.5×10^{-3}	2.97	6.8×10^{10}	–	E1	c2 $^4P^e_{5/2}$–c5 $^4D^o_{7/2}$	191.007 ± 0.184	–

Table 4. Measured and predicted lifetimes for some of the levels in Fe XII. Measured values from M01: Moehs et al. (2001); T02: Träbert et al. (2002). The predicted values have been calculated here with SUPERSTRUCTURE and adjusted energies. Note the excellent agreement.

i	Upper level	Measured (ms)	This work (ms)
2	$3s^2\ 3p^3\ ^2D^o_{3/2}$	20.3±1.2 (M01) – 18.0±0.1 (T02)	17.7
3	$3s^2\ 3p^3\ ^2D^o_{5/2}$	306±10 (T02)	310.8
4	$3s^2\ 3p^3\ ^2P^o_{1/2}$	4.4±0.4 (M01) – 4.1±0.12 (T02)	3.8
5	$3s^2\ 3p^3\ ^2P^o_{3/2}$	1.85±0.24 (M01) – 1.70±0.08 (T02)	1.6

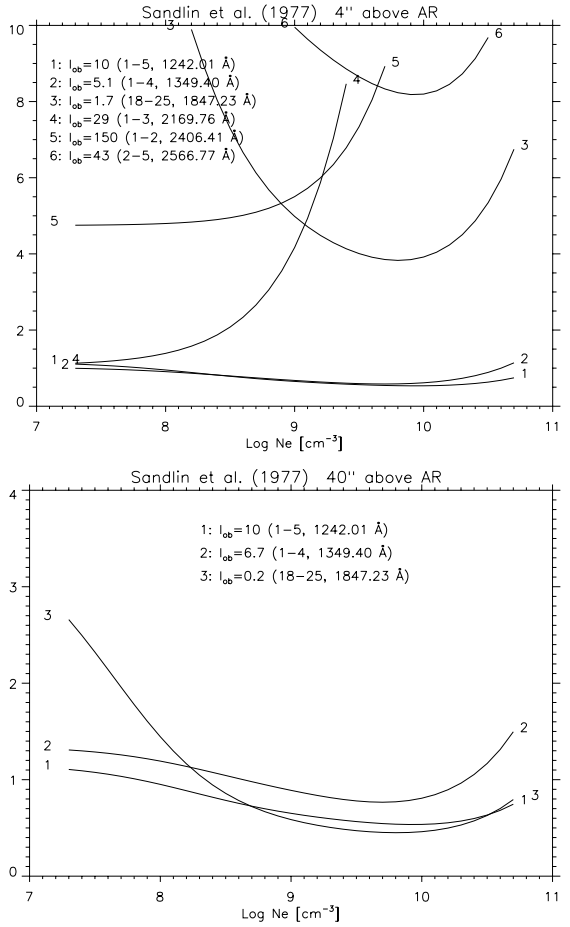

Fig. 1. The F_{ji} curves relative to the Skylab ATM observations 4″ (*top*) and 40″ (*bottom*) above an active region reported by Sandlin et al. (1977). For each line, we indicate: the observed intensities $I_{\rm obs}$; the lower and upper level index corresponding to Table 2; the theoretical wavelength. The large disagreements at 4″ could be due to blending and to calibration errors at the longer wavelengths.

The other bright forbidden lines fall at wavelengths longward of 1600 Å. Unfortunately the wavelength region above 1600 Å (including the visible) is still almost entirely unexplored, in terms of coronal forbidden lines. As far as we are aware, there are no other published off-limb measurements with calibrated line intensities other than those obtained with the NRL Skylab spectrometer by Sandlin et al. (1977) and Feldman & Doschek (1977). Various instruments such as the HRTS and the Solar Maximum Mission UVSP performed observations at these wavelengths, but limited to small spectral ranges or close to the solar limb.

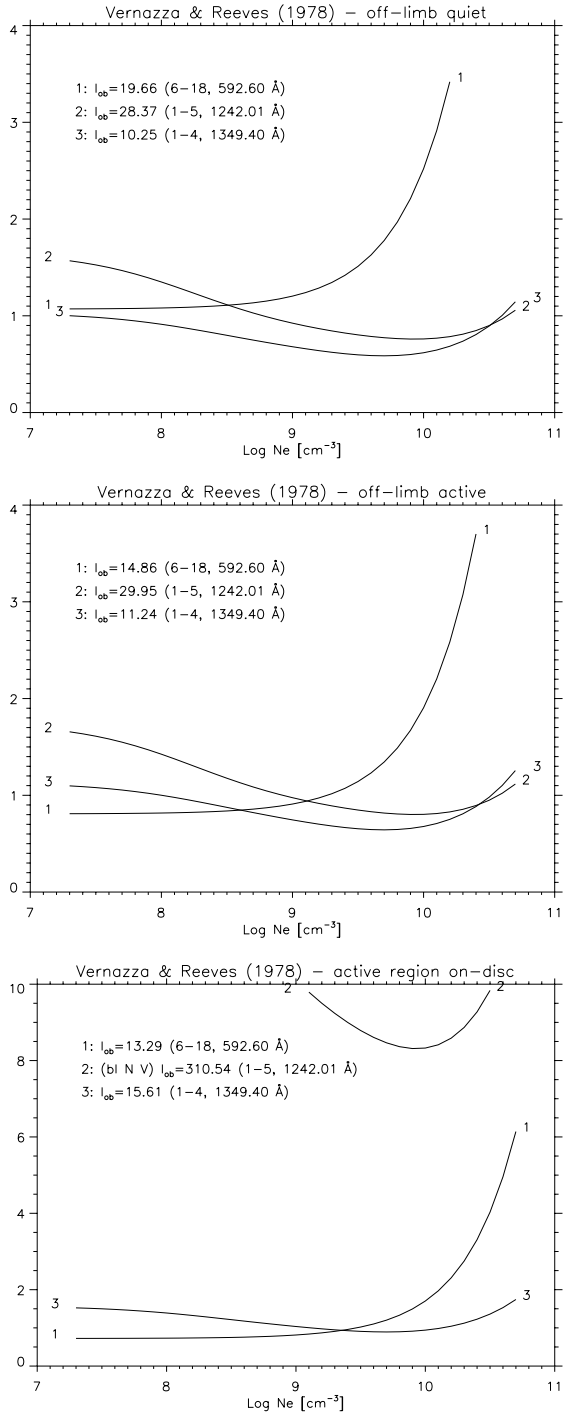

Fig. 2. F_{ji} curves relative to the Skylab observations of Vernazza & Reeves (1978). From top to bottom: off-limb quiet, off-limb active and average on-disk active region.

Table 5. Summary of the line identifications for Fe XII. The columns indicate: 1) the indices corresponding to Table 2; 2) the relative intensity (at 10^8, 10^{12} cm^{-3}, and log T[K] = 6.15), scaled to the brightest line; 3) the wavelengths calculated from our best energies $E_{\rm best}$; 4) observed wavelengths $\lambda_{\rm observed}$ (unless specified otherwise values are from Behring et al. 1976); some details are indicated (bl = blend; bl-mr = blend in medium-resolution spectra; bl-w = blend with a weak line; U = previously unpublished); lines with no or a tentative identification have a question mark; 5 and 6) previous original identifications consistent or not with ours (with observed wavelengths in Å; note that observed and calculated wavelengths in the cited literature can differ from the values reported here). The last column indicates new (N) or revised (R) identifications, and if a spectral line is only visible in high-density plasmas (H). Legenda: BRW67: Burton et al. (1967); B78: Bromage et al. (1978); D99: Del Zanna (1999); F67: Fawcett et al. (1967); F70: Fawcett (1970); F71: Fawcett (1971); G66: Gabriel et al. (1966); G71: Gabriel et al. (1971); Je71: Jefferies et al. (1971); J71: Jordan (1971); J93: Jupen et al. (1993); S71: Svensson (1971); SBT77: Sandlin et al. (1977); T98: Trabert (1998).

$i-j$	*Int* 10^8	*Int* 10^{12}	$\lambda_{\rm best}$(Å)	$\lambda_{\rm observed}$(Å)	Same ID	Diff. ID	
3–40	2.5×10^{-4}	6.8×10^{-3}	179.259 ± 0.007	179.266 ± 0.01 (U)	B78		H, R
1–32	3.0×10^{-3}	8.1×10^{-3}	186.241 ± 0.003	186.248 ± 0.01 (U)			H, N
2–36	1.0×10^{-2}	0.19	186.854 ± 0.004	186.854 ± 0.002 (B78, bl mr)	B78		
3–39	5.3×10^{-2}	0.31	186.887 ± 0.007	186.887 ± 0.005 (U, bl mr)	G66, B78		H, R
4–41	1.1×10^{-3}	6.8×10^{-2}	188.170 ± 0.018	188.17 ± 0.01 (U)		F71, B78(188.216)	H, N
1–31	5.8×10^{-3}	8.6×10^{-3}	190.068 ± 0.004	190.06 ± 0.01 (B78)	B78		H
5–41	3.3×10^{-4}	2.1×10^{-2}	190.467 ± 0.018	190.459 ± 0.01 (B78)	B78		H
6–84	1.8×10^{-2}	7.5×10^{-3}	191.007 ± 0.184	? 191.045 ± 0.01			N
5–40	5.0×10^{-3}	0.14	191.049 ± 0.008	191.049 ± 0.01 (U)	F71		H
1–30	0.32	0.10	192.394 ± 0.002	192.394 ± 0.002	F67		
1–29	0.67	0.21	193.509 ± 0.002	193.509 ± 0.002	F67		
2–34	9.3×10^{-4}	6.2×10^{-3}	194.903 ± 0.002	? 194.92 ± 0.01 (B78)			H
1–27	1.0	0.32	195.119 ± 0.002	195.119 ± 0.002 (bl mr)	F67(195.14)		R
2–33	3.9×10^{-3}	9.1×10^{-2}	195.179 ± 0.002	195.179 ± 0.002 (U, bl mr)	F71(195.2)		H, R
3–34	1.8×10^{-2}	0.12	196.640 ± 0.002	196.640 ± 0.01 (bl mr Fe XIII)	B78		
3–33	6.7×10^{-4}	1.6×10^{-2}	196.921 ± 0.002	196.923 ± 0.01 (B78)	B78		H
4–37	5.4×10^{-4}	2.3×10^{-2}	198.581 ± 0.008	198.58 ± 0.01	F71	B78	H
5–37	1.5×10^{-3}	6.4×10^{-2}	201.140 ± 0.008	201.14 ± 0.01	F71	B78	H
4–35	1.0×10^{-3}	4.2×10^{-2}	201.740 ± 0.021	201.74 ± 0.01 (bl)	F71		H
5–38	4.6×10^{-4}	3.8×10^{-2}	201.760 ± 0.009	201.75 ± 0.01 (U, bl)			H, N
3–32	3.2×10^{-2}	8.7×10^{-2}	203.728 ± 0.005	203.728 ± 0.004 (bl Fe XIII mr)		B78 (203.272)	N
2–31	1.2×10^{-2}	1.7×10^{-2}	206.368 ± 0.005	? 206.369 ± 0.01 (bl?)	B78		
3–31	8.7×10^{-3}	1.3×10^{-2}	208.316 ± 0.005	? 208.318 ± 0.01 (B78 bl?)	B78		H
2–30	1.5×10^{-2}	5.0×10^{-3}	209.113 ± 0.003	–			
5–34	1.9×10^{-3}	1.3×10^{-2}	210.918 ± 0.003	? 210.932 ± 0.01 (B78)	B78		H
2–28	9.3×10^{-3}	4.6×10^{-2}	211.732 ± 0.005	? 211.738 ± 0.01	F71		H
3–27	1.6×10^{-2}	5.2×10^{-3}	214.399 ± 0.003	214.405 ± 0.01		J93(214.416)	N
2–26	7.1×10^{-3}	5.1×10^{-2}	217.276 ± 0.015	? 217.271 ± 0.01	F71		H
3–26	1.7×10^{-2}	0.12	219.437 ± 0.015	219.438 ± 0.004 (bl?)	F71		
1–22	1.9×10^{-2}	1.6×10^{-2}	221.410 ± 0.049	221.41 ± 0.01 (bl S XII)			N
3–24	1.9×10^{-3}	1.7×10^{-2}	223.000 ± 0.100	223.0 ± 0.2 (? T98)			H, N
1–17	1.5×10^{-2}	2.9×10^{-2}	225.572 ± 0.254	? 225.856 ± 0.004 (bl)			N
5–28	3.2×10^{-3}	1.6×10^{-2}	230.768 ± 0.006	? 230.78 ± 0.01 (U)	B78		H, R
3–23	2.0×10^{-2}	2.7×10^{-2}	240.740 ± 0.059	240.74 U (bl 240.713 Fe XIII)			N
3–19	2.6×10^{-2}	4.1×10^{-2}	249.388 ± 0.032	249.388 ± 0.01 (bl?)			N
3–16	4.0×10^{-2}	2.6×10^{-2}	256.410 ± 0.066	256.41 ± 0.01 U (bl Fe XIII)			N
2–14	1.6×10^{-2}	9.9×10^{-3}	259.495 ± 0.068	? 259.494 ± 0.002 (bl S X)			N
3–15	1.2×10^{-2}	7.4×10^{-3}	259.963 ± 0.068	? 259.963 ± 0.002 (bl S X?)			N
2–12	6.0×10^{-3}	3.3×10^{-2}	283.443 ± 0.017	283.446 ± 0.008 (J93)	F71(283.64 bl), J93		H
2–11	2.9×10^{-3}	9.7×10^{-3}	287.221 ± 0.017	? 287.226 (J93)	J93		H
3–11	2.5×10^{-2}	8.4×10^{-2}	291.010 ± 0.018	291.01 ± 0.01 (bl Fe XIV)	F71		
5–13	4.5×10^{-3}	3.1×10^{-2}	303.135 ± 0.019	? 303.135 ± 0.008 (J93)	J93		H
4–12	2.8×10^{-3}	1.5×10^{-2}	312.253 ± 0.020	? 312.255 ± 0.008 (J93)	J93		H
2–9	1.6×10^{-2}	6.7×10^{-2}	335.380 ± 0.035	335.38 ± 0.01 (U, bl Fe XVI, Mg VIII)	J93	F71 (335.06)	R
3–10	2.3×10^{-2}	9.6×10^{-2}	338.263 ± 0.013	338.263 ± 0.01	F70(338.27)		
1–8	9.0×10^{-2}	3.5×10^{-2}	346.852 ± 0.006	346.852 ± 0.01	F71		
1–7	0.18	7.3×10^{-2}	352.106 ± 0.006	352.107 ± 0.01	F71		

Table 5. continued.

$i-j$	*Int* 10^8	*Int* 10^{12}	λ_{best}(Å)	$\lambda_{observed}$(Å)	Same ID	Diff. ID
1–6	0.31	0.12	364.467 ± 0.007	364.467 ± 0.004	F71	
5–10	4.5×10^{-3}	1.9×10^{-2}	382.847 ± 0.016	382.83 ± 0.01 (F71)	F71	H
6–18	2.3×10^{-2}	1.4×10^{-4}	592.600 ± 0.123	592.6 ± 0.1 (D99)		N
1–5	5.6×10^{-2}	7.5×10^{-3}	1242.01 ± 0.01	1242.00 ± 0.01 (SBT77, bl?)	BRW67	
1–4	3.2×10^{-2}	2.1×10^{-3}	1349.40 ± 0.02	1349.40 ± 0.01 (SBT77)	BRW67	
18–25	1.1×10^{-3}	1.7×10^{-4}	1847.23 ± 11.19	1847.25 (SBT77, bl?)		N
1–3	0.19	1.2×10^{-4}	2169.76 ± 0.05	2169.08 ± 0.02 (SBT77, air; 2169.76 vacuum, bl Ni III)	G71, J71, S71	
1–2	0.32	1.7×10^{-3}	2406.41 ± 0.06	2405.68 ± 0.01 (SBT77, air; 2406.41 vacuum, bl Fe II)	SBT77	
2–5	3.2×10^{-2}	4.4×10^{-3}	2566.77 ± 0.13	2565.93 ± 0.06 (SBT77, air; 2566.70 vacuum, bl Fe II,?)	SBT77	
3–5	1.3×10^{-2}	1.8×10^{-3}	2904.70 ± 0.17	–		
2–4	1.2×10^{-2}	8.0×10^{-4}	3072.06 ± 0.19	3072. (Je71 air; 3072.9 vacuum)	J71, S71	
16–18	4.5×10^{-3}	2.7×10^{-5}	14 218.7	–		

Table 6. Intensity ratios (ergs) of the 1242 and 1349.4 Å lines and electron densities N_e (cm^{-3}) for different sources. SBT77: Skylab NRL-ATM off-limb observations reported by Sandlin et al. (1977); FD77: Skylab NRL-ATM off-limb observations reported by Feldman & Doschek (1977); VR78: Skylab Harvard-ATM off-limb observations reported by Vernazza & Reeves (1978); S86: HRTS and Skylab NRL-ATM observations of an active region (plage), a sunspot (umbra) and at the solar limb, reported by Sandlin et al. (1986); C94: active regions (AR) and flare on-disc/limb observations with the Skylab NRL-ATM reported by Cook et al. (1994); S: SOHO/SUMER off-limb observations (see text); J01: HST/STIS stellar observations reported by Jordan et al. (2001).

SBT77 4″	SBT77 40″	FD77 A(40″)	FD77 B(40″)	VR78 quiet	VR78 active	S86 plage	S86 umbra	S86 limb	C94 AR	C94 flares	S 30″	J01
2.0	1.5	1.6	1.4	2.8	2.7	2.0	2.7	3.7	2.1–2.9	2.3–3.2	1.4	1.9
4×10^8	–	–	–	3.5×10^{10}	2.9×10^{10}	4×10^8	2.9×10^{10}	3.6×10^{11}	5×10^9–4×10^{10}	10^{10}–7.6×10^{10}	–	3×10^8

Unfortunately all the Fe XII lines long-ward of 1600 Å are swamped by chromospheric lines (mostly Fe II), in solar on-disk and near-limb observations, as discussed by Feldman et al. (1983). The amount of blending depends on the distance from the solar limb, and is difficult to assess. Another large uncertainty is in the radiometric calibration of the NRL Skylab spectrometer at the longer wavelengths.

Blending and an inaccurate calibration could be the reasons for the large inconsistencies in the F_{ji} curves relative to the Sandlin et al. (1977) observations taken at 4″ off-limb shown in Fig. 1. Feldman et al. (1983) pointed out that the 4″ off-limb observations presented by Sandlin et al. (1977) could not have been taken so close to the limb because in that case strong blending with chromospheric lines should be present. On the other hand Feldman et al. (1983) only considered the ratio between the 2169 and 2406 Å lines (which gives a reasonable density of log N_e = 9.2 cm^{-3}), and did not consider the ratios between these lines and the lines at shorter wavelengths.

The situation improves at larger distances from the limb. Fig. 3 shows the F_{ji} curves relative to the NRL Skylab observations recorded 40″ off-limb reported by Feldman & Doschek (1977). There is a satisfactory agreement between these observations and theory, with the exception of the weak 2566.7 Å line, which is most probably still severely blended with Fe II emission.

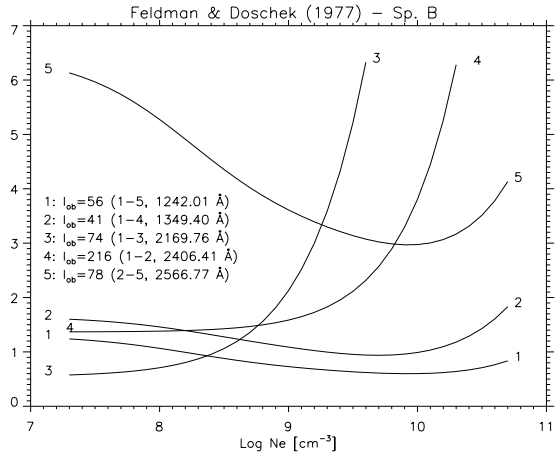

Fig. 3. The F_{ji} curves relative to the Skylab ATM observations reported by Feldman & Doschek (1977). The large disagreement for the 2–5 line is probably due to blending and to calibration errors at the longer wavelengths.

In summary, the forbidden lines of the ground configuration offer limited density diagnostics. The lines long-ward of

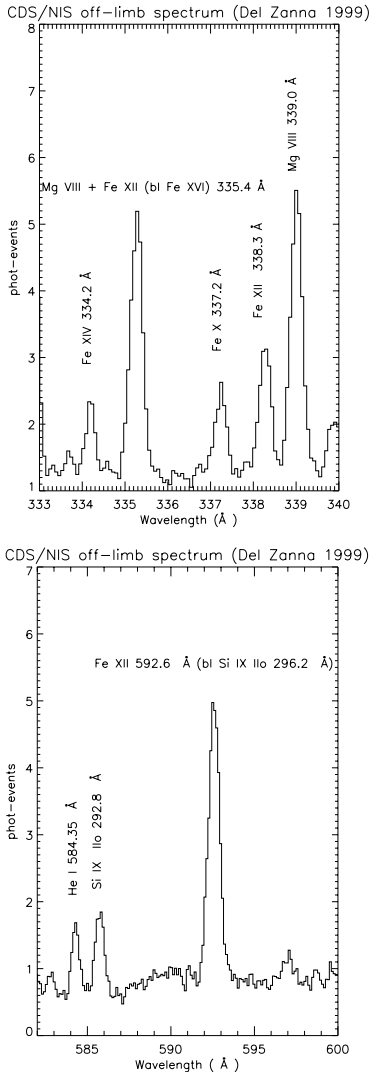

Fig. 4. SOHO CDS NIS spectra taken in a quiet-Sun off-limb region (Del Zanna 1999) and showing the newly identified Fe XII lines, most notably the electric quadrupole transition at 592.6 Å.

1600 Å are difficult to assess due to the few observational data available. The 1242, 1349 Å lines alone can only provide measurements at high densities, i.e. for solar flares.

4.3. Transitions $3s\,3p^4$–$3s^2\,3p^2\,3d$

Only one transition is predicted to be bright, in particular at low (coronal) densities. It is the 6−18 $^4P_{5/2}$–$^4F_{9/2}$ electric quadrupole transition. This transition is of particular importance for a large number of reasons. First, it is the only bright forbidden transition visible at EUV wavelengths. Second, its ratio with any of the other EUV dipole-allowed transitions provides a good density diagnostic at $N_e > 10^9$ cm^{-3}. Third, its ratio with any of the UV forbidden lines is an excellent density diagnostic over a large range of densities. Fourth, at quiet Sun coronal densities this line is as bright as the well known 3−10 (338.263 Å) line (see Fig. 4). Fifth, it turns out that at moderate resolution this line blends the important Fe XIX 592.2 Å flare line.

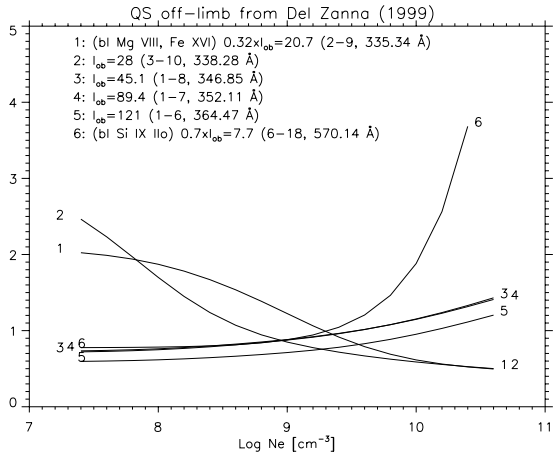

Fig. 5. F_{ji} curves relative to a quiet sun off-limb SOHO/CDS NIS observation (Del Zanna 1999) and the Del Zanna et al. (2001) calibration with the newly identified 6−18 592.6 Å line. Note the excellent agreement. Densities from ions emitted at similar temperatures are in the range log N_e = 8.7−8.8 cm^{-3}.

The upper $^4F_{9/2}$ level has not previously been identified, in fact neither have any of the relatively pure ^4F_J levels (14, 15, 16). After various analyses, we have found a very good match between the theoretical fine-structure splittings and the wavelengths of some lines.

We have identified the 6−18 transition with the 592.6 Å line, previously reported as unidentified in almost all solar observations (e.g. Skylab, see Vernazza & Reeves 1978; SOHO/CDS NIS, see Del Zanna 1999; and SOHO/SUMER in second order, see Feldman et al. 1997). In SOHO/CDS spectra (see Fig. 5), a minor complication is due to a blending with two second order Si IX transitions (according to the Del Zanna et al. 2001 calibration).

We have considered one of the quiet sun off-limb SOHO/CDS observation (see Del Zanna 1999 and Del Zanna et al. 2001), for which we know that the Si IX contribution is about 30%. We have removed this contribution from the observed line intensity, and plotted the F_{ji} curve in Fig. 5. The agreement between observation and theory is excellent, considering the uncertainties in the calibration.

The electric quadrupole transition, in conjunction with the forbidden lines in the UV is one of the best Fe XII density diagnostics for the quiet solar corona. We have seen that the forbidden lines in the UV are strongly blended with cooler lines or have diagnostics limited at high densities. It has been suggested by some authors (e.g. Keenan et al. 1990) that good density measurements from Fe XII lines could be obtained from the ratios of the intensities of the UV forbidden lines (e.g. the strongest 1242 Å line) with those observed in the EUV (e.g. the strongest 195 Å). However, no simultaneous observations existed, and indirect evidence was used to compare theoretical values with the observed ones. In general, aside from the difficulty of cross-calibrating two different instruments observing such different wavelengths, there is also the problem that such ratios also have a temperature dependence. For example, a 25% change in the temperature results in about a 30% change in the theoretical 1242, 195 Å ratio.

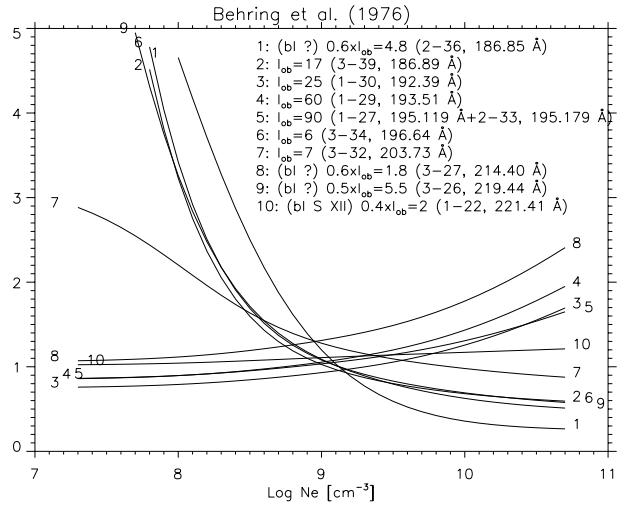

Fig. 6. The F_{ji} curves of the Behring et al. (1976) whole Sun observations.

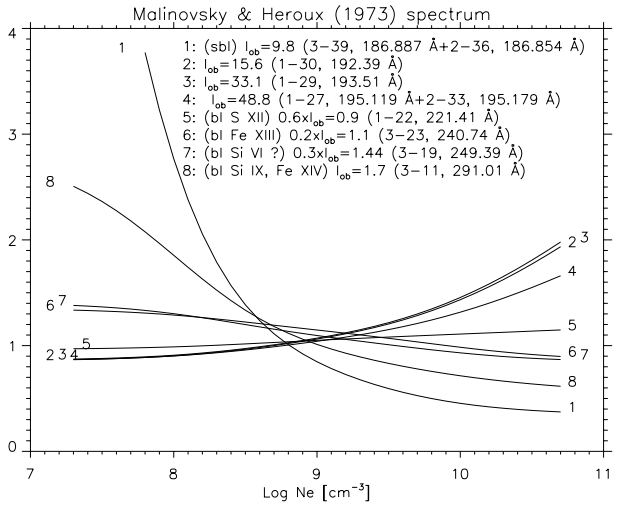

Fig. 7. The F_{ji} curves relative to the full-Sun spectrum of Malinovsky & Heroux (1973). The agreement between our present model and the observations is excellent. The curves also indicate an electron density $\log N_e = 8.8$ cm^{-3}, in excellent agreement with the values derived from other ions.

On the other hand, the EUV electric quadrupole 592.6 Å can easily be observed simultaneously with the UV forbidden lines. The ratio is only slightly temperature dependent. For example, a 25% change in the temperature results in only a 10% change in the theoretical ratios between this line and one of the UV lines. These ratios are an excellent density diagnostic since they vary by one order of magnitude in the 10^7–10^{11} cm^{-3} range.

Figure 2 shows the F_{ji} curves relative to the Skylab off-limb observations of Vernazza & Reeves (1978), that included the 592.6 Å line. The agreement between observation and theory is very good, and the derived densities have the expected values. Obviously, at large distances from the limb, photo-excitation and doppler dimming effects complicate the diagnostics.

4.4. Transitions $3s^2\ 3p^3$–$3s^2\ 3p^2\ 3d$

The brightest Fe XII lines are found in the EUV, in the 180−200 Å range (see Table 3 and Fig. 6). One complication is that, in most medium-resolution spectra, many of these lines are blended. For example, the strongest 1−27 195.119 Å line is blended, at high-densities, with the 2−33 line (we report a previously-unpublished measurement of 195.179 Å). The 3−39 186.887 Å transition is also blended (this time at all densities) with another Fe XII line, the 2−36 at 186.854 Å. Also in this case we report new accurate wavelength measurements. These lines are blended in most solar spectra. However, in the high-resolution spectra of Behring et al. (1976), these two lines are separated (note that the authors incorrectly identified one of the lines as due to S XI). The weaker 186.854 Å is possibly blended with an unknown transition (the S XI 186.84 Å is a relatively weak transition).

Finally, in medium-resolution spectra, the bright 3−34 196.640 Å transition is also blended with an Fe XIII 196.54 Å line. The only two bright unblended lines are the 1−30 192.394 Å and 1−29 193.509 Å lines.

After considering the presence of blends, the agreement between our present model and the Malinovsky & Heroux (1973) observations is excellent, as shown in Fig. 7. The 192.394, 193.509, 195.11 Å lines have almost the same density dependence, are bright and are unblended, hence they can reliably be used for instrument calibration purposes. For example, measurements of these lines could provide an independent check on the Solar-B/EIS radiometric calibration (the response of the Solar-B/EIS multi-layer happens to be highly peaked and centred at 195 Å). We note that the SOHO/GIS calibration presented by Del Zanna et al. (2001) will need to be revised in light of the new atomic data. However, Fig. 8 clearly shows that adjustments will only be minor, and within the stated accuracy (30%) of the absolute calibration.

As noted by previous authors, the 186.8 Å lines are an excellent density diagnostic for the quiet solar corona. Their intensities from Malinovsky & Heroux (1973) suggest a $\log N_e = 8.8$ cm^{-3}, in excellent agreement with the electron densities derived from other ions (see Paper I for Fe X), and in stark contrast to the results from previous measurements, as discussed in Storey et al. (2005).

The fifth strongest low-density transition (the 3−32 E1 transition, also predicted to be bright at high-densities) was identified by Bromage et al. (1978) with a line observed at 203.272 Å in laboratory spectra. However, no corresponding line is observed in the solar spectra, as it should. Nearby solar lines are observed at 203.173 and 203.728 Å, both being present in laboratory spectra at the same wavelengths, the latter being stronger in laboratory spectra. The other lines decaying from level 32 ($^2D^e_{5/2}$ but strongly mixed), or belonging to the same transition array, are predicted to be much weaker and would be hardly observable under any circumstances (B78 gave a tentative identification of the 2−32 with the 201.493 Å, and of the 5−32 with a 218.562 Å line). As discussed elsewhere, we agree on the identification given by Jupen et al. (1993) that the 203.173 Å line is due to Fe XIII. We therefore identify the 3−32 transition with the 203.728 Å line. Although Behring et al. (1976)

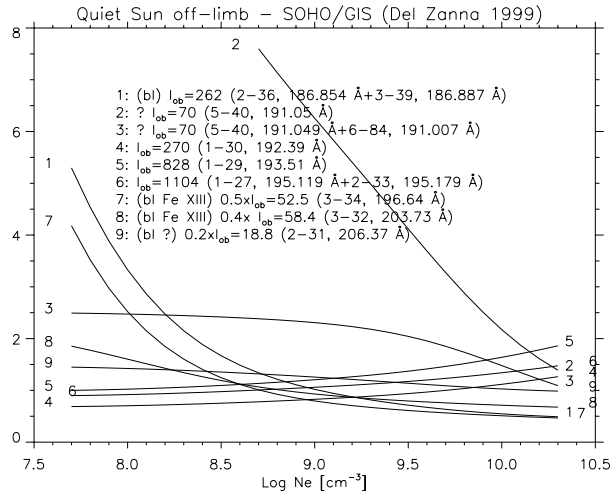

Fig. 8. The F_{ji} curves relative to a quiet Sun off-limb SOHO/GIS observation (Del Zanna 1999) and the Del Zanna et al. (2001) calibration.

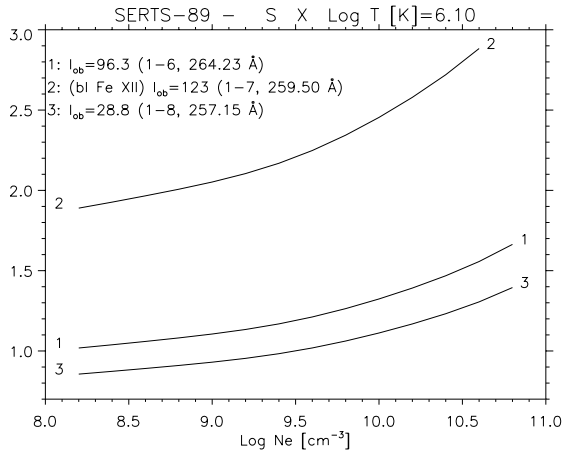

Fig. 9. F_{ji} curves relative to the SERTS-89 calibrated data of Thomas & Neupert (1994).

only provided indicative intensities, all the above-mentioned lines are close in wavelength, and considering the instrumentation used, large calibration effects are not expected. Indeed, Fig. 6 shows a good agreement between observation and theory. It should be noted that the strong 3−32 transition in any medium-resolution spectra is blended with two Fe XIII lines, often used for density-diagnostic purposes. The theoretical splitting of level 31 ($^2D^e_{3/2}$) is in excellent agreement with the wavelength of the weaker 2−31 line (206.368 Å).

The sixth-strongest transition (3−16) should only be observable in low-density plasmas. It is one of the strongest lines produced by one of the many previously-unidentified levels (in this case the $^4F^e_{7/2}$). The fine-structure splitting of the ^4F_J levels and the identification of the 592.6 Å line suggest that the 3−16 transition should fall around 256−257 Å. This line could be identified with the 256.925 Å line, that was tentatively identified by Behring et al. (1976) and all following authors as an Fe XV transition (current atomic data, see CHIANTI v.4, Young et al. 2003, suggest that this is not the case). The other option that we choose is that the 3−16 blends with an Fe XIII transition to form the observed 256.41 Å line (see Fig. 10). Indeed current Fe XIII atomic data (CHIANTI v.4) suggest that Fe XIII cannot contribute alone to the observed line. Note that in medium-resolution spectra the 256.41 Å line is blended with many other transitions.

The other lines from the ^4F_J levels are relatively weak. We identify the 2−14 transition as a blend with a bright S X line observed at 249.49 Å. Current atomic data for S X which include *R*-matrix calculations for this ion (see CHIANTI v.4) in fact suggest that the observed line is almost a factor of two brighter than the S X transition (see Fig. 9). The blend with the Fe XII transition does not completely solve this discrepancy, however. Finally, the 3−15 line is even weaker and most probably blends an unidentified line at 259.96 Å.

The seventh-strongest transition (3−11) is another interesting example. Levels 11 and 12 ($^2P^e_{3/2,1/2}$) were first identified by Fawcett (1971) using the 3−11 (290.99 Å, bright, as expected, also in high-density plasmas) and 2−12 (283.64 Å) lines, observed in the laboratory spectra. However, Jupen et al. (1993) identified the 4−12 transition with a laboratory line observed at 312.255 Å, and the 2−11 with a line observed at 287.226 Å. The authors obtained the energy splittings from the available NIST values, and accordingly revised the energies of the $^2P^e_{3/2,1/2}$ levels, giving a value of 389 668.0 ± 20 cm^{-1} for the $^2P_{3/2}$ level (3−11 291.053 and 2−11 287.226 Å). When we use the revised values for the energies of the ground configuration, we obtain instead a value of 389 733.0 cm^{-1}, giving wavelengths (3−11 291.01 and 2−11 287.22 Å) in excellent agreement with the observed values. Note that in solar spectra the 3−11 291.0 Å blends with Fe XIV and the 2−12 283.64 Å is too weak to be observed.

The 3−27 line has been observed as expected at 214.405 Å but the 2−30 has not. It should be observed at 209.12 Å. The 3−26 at 219.438 Å is a strong line in laboratory spectra, but in solar spectra is weak and is most probably blended with an unidentified line.

Level 19 ($^4D^e_{7/2}$) is strongly mixed. It is predicted to produce a line due to the transition 3−19, observable in both solar and laboratory spectra. We tentatively identify the 3−19 transition with the line observed in laboratory spectra at 249.37 Å. Note, however, that in solar spectra the line at 249.39 Å (previously unidentified) is most probably a blend.

The $^4D^e$ levels (20, 21, 22, 23) have not been previously identified. Our model predicts the brightest lines to be the 1−22 and 3−23 at low and high densities, respectively. These lines should fall at approximately 221 and 240 Å. We tentatively identify the first with the 221.41 Å solar line (blended with S XII), also observed in laboratory spectra at 221.43 Å. The 3−23 transition would be blending the stronger Fe XIII line observed at 240.713 Å (Be76 reported the presence of a blend).

The $^2G^e_{7/2,9/2}$ levels (24, 25) are relatively pure but have not been previously identified, because they give rise to weak lines. We propose to identify the 3−24 ($^2D_{5/2}$−$^2G_{7/2}$) dipole-allowed transition with a line observed in the laboratory at 223 Å. We note that there must be a typo in Table 3 of Trabert (1998), where this line is listed as observed at 233.1 Å. Based on the

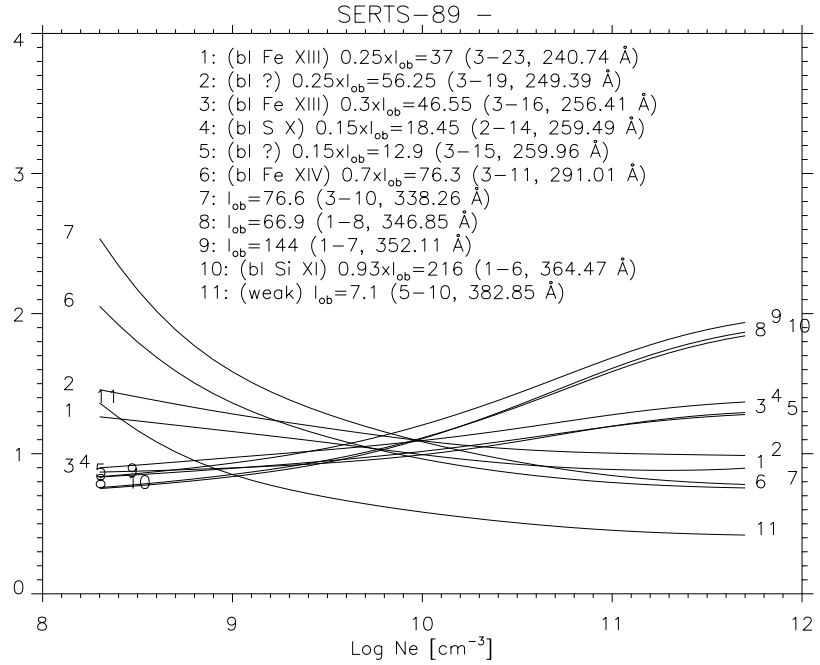

Fig. 10. F_{ji} curves relative to the SERTS-89 calibrated data of Thomas & Neupert (1994).

theoretical fine-structure splitting of the ^2G_J levels, we identify the 18−25 forbidden transition with a previously unidentified coronal line at 1847.25 Å (cf. Fig. 1). We note that this line can provide good density diagnostic at coronal densities ($\log N_e = 7-9$) when observed in conjunction with the brighter 1242, 1349 Å lines.

4.5. Transitions from the 3s 3p^3 3d levels

According to our model, all the transitions from the 3s 3p^3 3d levels are predicted to be weak, at low and high densities. Only few should be observable. Among them, the brightest one is the dipole-allowed 6−84 $^4P^e_{5/2}$–$^4D^o_{7/2}$ of the 3s 3p^4–3s 3p^3 3d transition array. We tentatively identify this transition with the 191.045 Å line observed in solar spectra (Behring et al. 1976) and previously identified with the 5−40 $^2P_{3/2}$–$^2D_{5/2}$ line. In fact the 5−40 line, although quite strong at high densities (hence visible in the laboratory spectra), is very weak at solar coronal densities. Figure 8 shows that the 5−40 line (number 2 in the figure) is about one order of magnitude weaker than the observed line. A blending of the 5−40 and the 6−84 lines (number 3 in the figure) brings its intensity into closer agreement.

4.6. Transitions 3s^2 3p^3 – 3s 3p^4

Lines of the 3s^2 3p^3–3s 3p^4 transition array fall in the 300−450 Å range. The brightest lines are due to decays from the $^4P^e_J$ levels (6, 7, 8, at 364.467, 352.107, 346.852 Å) to the ground state. Their intensity ratios are approximately independent of the electron density, and these lines can be useful for instrument calibration. Their observed ratios are in excellent agreement with the current atomic dataset (see Storey et al. 2005 but also Figs. 5 and 10). Note that we confirm Young et al. (1998) suggestion that the 364.852 Å is blended with an Si XI transition, that however only contributes by 7% to the observed line.

The next brightest lines are the decays of the $^2D^e_J$ levels (9, 10), which produce the 3−10 (338.263 Å) and 2−9 lines. A ratio with any of the previous ones provides a good density diagnostic. We note that previous large discrepancies in density measurements with the 3−10 line are now corrected with the current atomic data (see Storey et al. 2005, for details).

The theoretical splitting of the $^2D^e_J$ suggests a wavelength for the 2−9 line in disagreement with the identification given by Fawcett (1971) with the line observed in the laboratory spectra at 335.06 Å (also present in solar ones). We suggest instead a wavelength of 335.38 Å, i.e. the 2−9 line is a blend with two other Fe XVI, Mg VIII lines. The Mg VIII line forms a branching ratio with a nearby unblended line, while the Fe XVI line is the brightest of the Fe XVI doublet. The other one is at 360.7 Å and is unblended. Hence, in both Mg VIII and Fe XVI cases, it is possible to accurately estimate the contributions to the observed line at 335.4 Å. Del Zanna (1999) and Del Zanna et al. (2001) used SOHO/CDS observations to suggest that the 2−9 line contributes significantly to the blend, whenever Fe XVI emission is absent. Indeed we confirm these estimates. We have removed the contribution from Mg VIII and Fe XVI and the results are plotted in Fig. 5. The agreement is satisfactory, considering the uncertainty in the current calibration (20−30%), but does not exclude the presence of a further minor blend.

Finally, we note that the 5−10 382.83 Å line is weak. Poor statistics could be the reason why there is disagreement between the predicted intensity of this line in the SERTS-89 spectrum (see Fig. 10).

5. Summary and conclusions

A comprehensive benchmark of Fe XII atomic data against available observations has been performed. All previous line

identifications have been reviewed, by comparing the results of our model with experimental data in a comprehensive way.

We confirm many previous identifications but also reject or revise some, and suggest many new ones. The most important one being the electric quadrupole $^4P^e_{5/2}$–$^4F^e_{9/2}$ transition with the bright coronal line observed at 592.6 Å. The fact that many new identifications are proposed is not surprising, considering that the entire model ion is significantly different from those previously published.

We have identified most of the previously unknown energy levels. The comparison between our observed energies and those of the scattering calculation is satisfactory, thus giving us further confidence in the collision strengths calculated by Storey et al. (2005).

The assessment also indicated the presence of many blends, and allowed uncertainties on the atomic data to be estimated. For the cases free of blends, the agreement between theoretical and experimental line intensities is excellent. The few laboratory measurements of metastable level lifetimes are also in good agreement with our calculations.

We have pointed out which are the best lines to be used for density diagnostics and instrument calibration purposes. The new atomic data provide electron densities significantly different from those published in the previous literature. This occurs for a variety of combination of spectral lines, and for a variety of density ranges. Some examples have been provided.

Further work and high-resolution spectral observations are needed to confirm the identification of the weaker transitions, and to assess blending of the UV forbidden lines.

Acknowledgements. Support from PPARC is acknowledged.
We warmly thank B. C. Fawcett for his encouragement and help. Also P. R. Young, J. Payne and J. Lang for help during visits at RAL.

References

Behring, W. E., Cohen, L., Doschek, G. A., & Feldman, U. 1976, ApJ, 203, 521
Binello, A. M., Landi, E., Mason, H. E., Storey, P. J., & Brosius, J. W. 2001, A&A, 370, 1071
Bromage, G. E., Fawcett, B. C., & Cowan, R. D. 1978, MNRAS, 183, 19
Burton, W. M., Ridgeley, W. M., & Wilson, A. R. 1967, MNRAS, 135, 207
Cook, J. W., Keenan, F. P., Harra, L. K., & Tayal, S. S. 1994, ApJ, 429, 924
Del Zanna, G. 1999, Ph.D. Thesis, Univ. of Central Lancashire, UK
Del Zanna, G., Bromage, B. J. I., Landi, E., & Landini, M. 2001, A&A, 379, 708
Del Zanna, G., Berrington, K. A., & Mason, H. E. 2004, A&A, 422, 731
Edlén, B. 1966, Metrologia, 2, 71
Eissner, W., Jones, M., & Nussbaumer, H. 1974, Comp. Phys. Commun., 8, 270
Fawcett, B. C. 1970, J. Phys. B Atom. Mol. Phys., 3, 1732
Fawcett, B. C. 1971, J. Phys. B Atom. Mol. Phys., 4, 1577
Fawcett, B. C., Gabriel, A. H., & Saunders, P. A. H. 1967, Proc. Phys. Soc., 89, 863
Feldman, U., & Doschek, G. A. 1977, J. Opt. Soc. Am., 67, 726
Feldman, U., Doschek, G. A., & Cohen, L. 1983, ApJ, 273, 822
Feldman, U., Behring, W. E., Curdt, W., et al. 1997, ApJS, 113, 195
Flower, D. R. 1977, A&A, 54, 163
Fuhr, J. R., Kelleher, D. E., Martin, W. C., et al. 1999, NIST Atomic Spectra Database ver. 2.0 (NIST Physical Reference Data)
Gabriel, A. H., Fawcett, B. C., & Jordan, C. 1966, Proc. Phys. Soc., 87, 825
Gabriel, A. H., Garton, W. R. S., Goldberg, L., et al. 1971, ApJ, 169, 595
Jefferies, J. T., Orrall, F. Q., & Zirker, J. B. 1971, Sol. Phys., 16, 103
Jordan, C. 1971, Sol. Phys., 21, 381
Jordan, C., McMurry, A. D., Sim, S. A., & Arulvel, M. 2001, MNRAS, 322, L5
Jupen, C., Isler, R. C., & Trabert, E. 1993, MNRAS, 264, 627
Keenan, F. P., Tayal, S. S., & Henry, R. J. W. 1990, Sol. Phys., 125, 61
Landman, D. A. 1978, ApJ, 220, 366
Malinovsky, L., & Heroux, M. 1973, ApJ, 181, 1009
Moehs, D. P., Bhatti, M. I., & Church, D. A. 2001, Phys. Rev. A, 63, 32515
Nussbaumer, H., & Storey, P. J. 1978, A&A, 64, 139
Sandlin, G. D., Brueckner, G. E., & Tousey, R. 1977, ApJ, 214, 898
Sandlin, G. D., Bartoe, J.-D. F., Brueckner, G. E., Tousey, R., & Vanhoosier, M. E. 1986, ApJS, 61, 801
Storey, P. J., Del Zanna, G., Mason, H. E., & Zeippen, C. J. 2005, A&A, 433, 717
Svensson, L. Å. 1971, Sol. Phys., 18, 232
Thomas, R. J., & Neupert, W. M. 1994, ApJS, 91, 461
Trabert, E. 1998, MNRAS, 297, 399
Träbert, E., Gwinner, G., Wolf, A., et al. 2002, J. Phys. B Atom. Mol. Phys., 35, 671
Träbert, E., Calamai, A. G., Gwinner, G., et al. 2003, J. Phys. B Atom. Mol. Phys., 36, 1129
Vernazza, J. E., & Reeves, E. M. 1978, ApJS, 37, 485
Young, P. R., Landi, E., & Thomas, R. J. 1998, A&A, 329, 291
Young, P. R., Del Zanna, G., Landi, E., et al. 2003, ApJS, 144, 135
Zeippen, C. J., Seaton, M. J., & Morton, D. C. 1977, MNRAS, 181, 527